

Self-Consistent Calculation of Electronic Energy Levels
in Quantum Heterostructures

A Major Qualifying Project Report

submitted to the Faculty

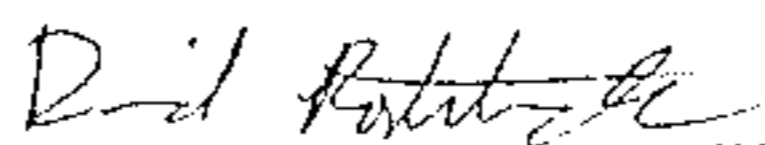
of the

WORCESTER POLYTECHNIC INSTITUTE

in partial fulfillment of the requirements for the

Degree of Bachelor of Science

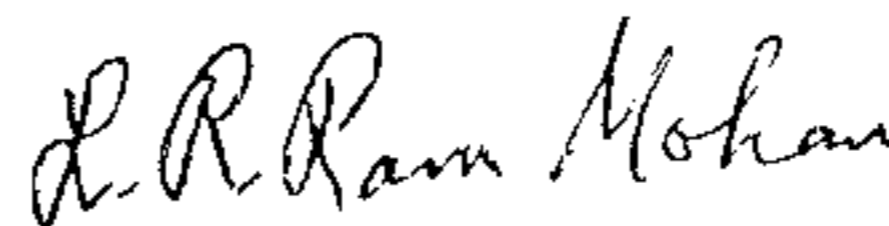
by



David J. Rostcheck

Date: April 17, 1992

Approved:



~~Professor L. Ramdas Ram-Mohan, Advisor~~

Abstract

The ability to fabricate semiconductor structures on an atomic scale introduces the potential for opto-electronic devices with truly quantum-mechanical properties. We need computational methods with sufficiently high accuracy that we can calculate the energy levels in such structures and compare results with direct spectroscopic observation. Further, in an active device the charge carriers redistribute themselves and alter the energy bands of the system. To obtain accurate device modeling, we solve the Schrodinger and Poisson equations until self-consistency is attained.

We present an accurate and compact scheme for obtaining the energy levels and the band-edge bending in planar compound semiconductor heterostructures of arbitrary composition using the finite element method with fifth order Hermite interpolation. Our method can account for the presence of an externally applied magnetic field either parallel or perpendicular to the layers, and is applicable in the presence of a perpendicular external electric field.

Acknowledgements

This project is dedicated to my father, James Nicholas Rostcheck, whose love I never doubted. I would like to thank specifically Dr. George Phillies for his unflagging support and dedication throughout my undergraduate years. I would also like to thank my project advisor, Dr. L. R. Ram-Mohan for his invaluable assistance. Finally, I express my gratitude to my family and to the members of the Physics department for their support.

Contents

1	Introduction	3
2	The Self-Consistency Problem	10
2.1	Poisson's Equation – FEM Formulation	10
2.2	Continuity Conditions	13
2.3	Source Terms in Poisson's Equation	16
2.4	Fermi Level Solution	21
3	FEM Boundary Conditions	22
4	The Hermite Interpolating Polynomials	27
5	Discussion of Results	30
5.1	Depletion Region Effects	31
5.2	Energy Level Shifting	32
5.3	Proposed Research	34
5.4	Numerical Issues	37
6	Conclusions	43

List of Figures

1	Planar Quantum Well	4
2	Quantum Well Conduction Band-Edge Profile	4

3	Self-Consistent Quantum Well	7
4	Iterative Self-Consistent Algorithm	8
5	Local and Global Element Indices	14
6	Finite Element Approximation	27
7	Quantum Well, Donor Density 10^{16}	39
8	Quantum Well, Donor Density 10^{17}	40
9	Quantum Well, Donor Density 10^{18}	41
10	Quantum Well, Donor Density 10^{19}	42

List of Tables

1	Approximate depletion region for 100 Å well with 320 meV bandgap	31
2	Approximate potential energy at well center relative to well edge.	32
3	Difference between first and second energy levels for high donor densities	32

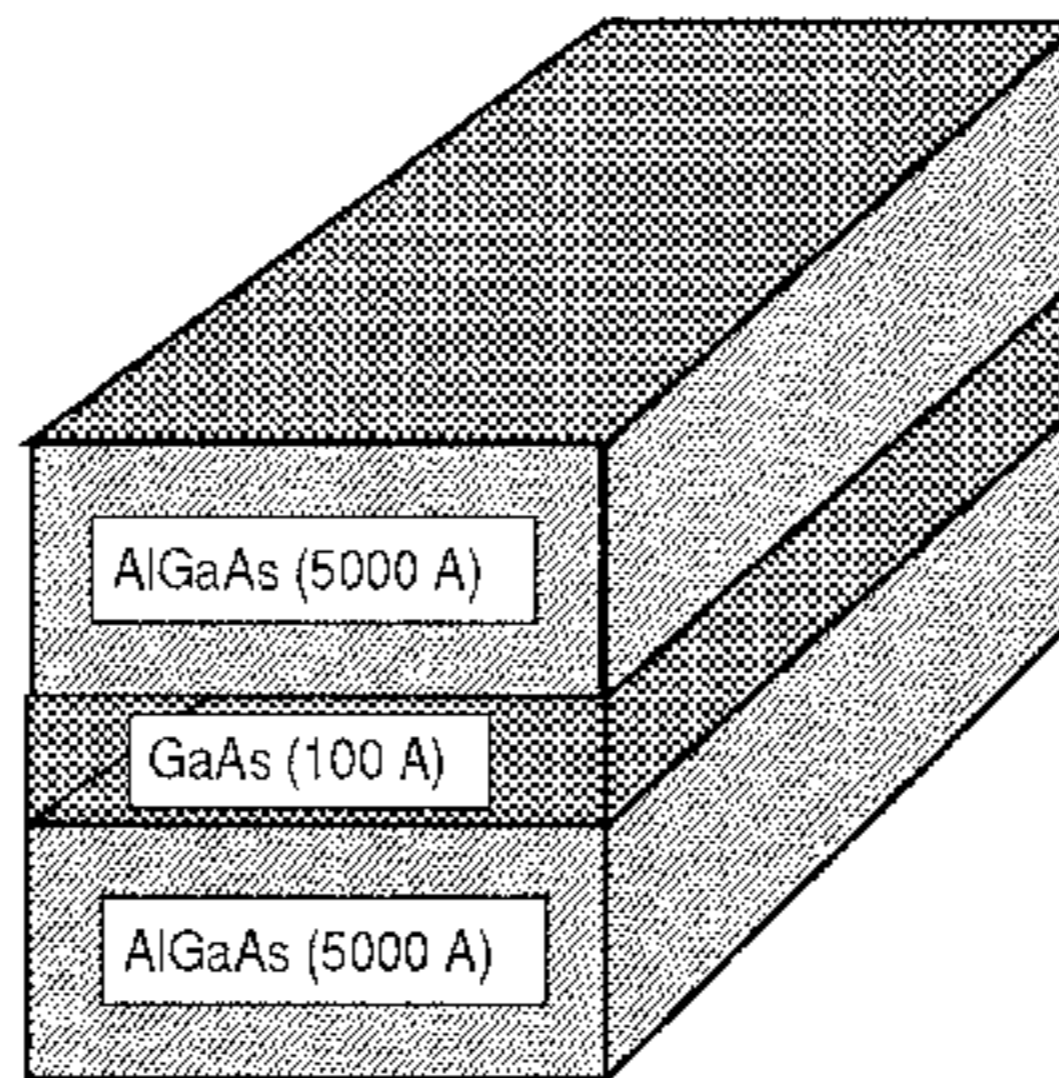
1 Introduction

The recent introduction of atomic-scale fabrication techniques, or “nanostructure fabrication”, makes possible the development of new optoelectronic devices. We consider two popular atomic scale structures: the quantum well and the superlattice. Present day fabrication techniques allow great control over the structure geometry and location of doped impurity atoms. Additionally, one may impose external magnetic or electric fields which affect the properties of the structure. We have developed algorithms which are capable of efficiently solving for the properties of such structures even under the presence of such external fields. We consider corrections due to the structure’s own self-consistent electric field and present an efficient and accurate algorithm for the self-consistent solution of electronic energy levels in atomic-scale structures.

The recently developed Molecular Beam Epitaxy (MBE) and Molecular Vapor Deposition (MOCVD) techniques allow one to construct structures essentially one atomic layer at a time. We refer to such structures of nanometer dimensions as *quantum* structures, since at dimensions comparable to 1000 Å quantum mechanical effects become significant and we can no longer use classical electromagnetic theory to predict electronic properties of the structure. Our work considers planar structures, constructed by depositing successive layers onto a substrate. We call these layered structures *heterostructures*. One constructs a *device* by connecting such a structure to an external voltage source.

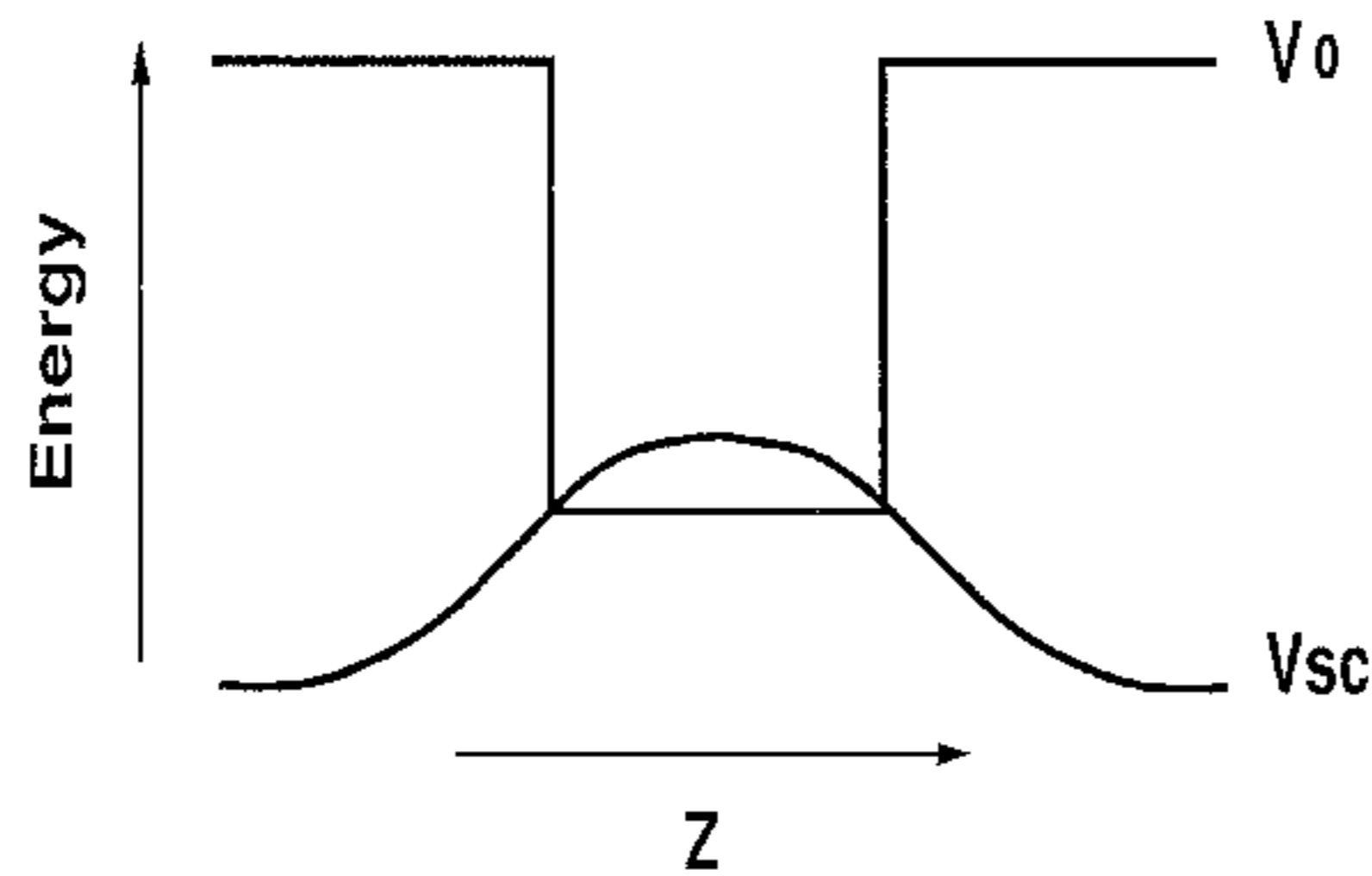
Two principle heterostructure types are the quantum well and the superlattice. The simple quantum well consists of two identical semiconductor layers separated by a middle layer of different composition (see figure 1). The middle material has a smaller bandgap

Figure 1: Planar Quantum Well



than the outer layers (see figure 2). More complicated structures, such as double wells or

Figure 2: Quantum Well Conduction Band-Edge Profile



V_0 is the ideal potential energy; V_{sc} is the self-consistent potential energy due to charge that has fallen into the well.

asymmetric wells, can also be constructed. The superlattice consists of a periodic sequence of semiconducting materials, usually of two different types, alternating in layers.

Our interest in structures of this nature lies in their optical and electronic properties. Heterostructure optical properties are of interest because of the quantum heterostructure's discrete energy eigenstates. While micrometer-scale semiconductor structures possess intrin-

insic energy bands, quantum heterostructures have discrete energy *levels*, which depend on the materials and geometry of the heterostructure. Such discrete levels produce photon emission or absorption with a sharply defined cutoff frequency. We can thus create quantum devices with specifically tailored electro-optic characteristics. For example, a micrometer-scale p-n junction can act as a photodiode since incident photons excite electrons from the valence to the conduction band, causing a current. A nanometer-scale device would be engineered to respond only to photons above specific cutoff frequency. Further, since the energy levels can easily be adjusted by the application of an external field, the frequency response of the detector can be tuned. The same concept allows the creation of tunable solid state lasers. The LED, a micrometer-scale device, can, if suitably driven, emit a range of light frequencies. Its nanometer-scale counterpart, the quantum well, can be made to emit light of sharply defined frequency. Because its energy states are multiple and discrete, the quantum well can be made to lase at particular frequencies; because the energy levels can be adjusted, the laser can be tuned. The ability to engineer a laser to emit at certain wavelengths is of great importance for fiber optic communications, since fiber optic cables have their own frequencies of maximum transmission which may not coincide with those of the traditional solid-state laser used to transmit through the fiber.

Heterostructure electronic properties arise primarily because of the geometry of the heterostructure and the control over donor doping. In practice, we construct semiconductors by introducing controlled amounts of impurities into otherwise pure material. The impurities donate either conduction electrons or holes, which carry the current. Such semiconductors are termed *impurity* semiconductors. They differ from *intrinsic* semiconductors, in which

only those electrons with thermal energy above the Fermi energy are available for conduction. For common semiconductors, only about one electron in 10^9 lies within this range. By introducing impurities of one part in 10^5 we greatly increase the current carrying capacity of the material. Through a process called modulation doping, or step-back doping, we can precisely control the donor density throughout the heterostructure. If we dope only the barriers in a quantum well and leave the well undoped, electrons from the barriers fall into the well and become trapped. They can then propagate along the channel with little scattering. Thus, we can create areas of high electron mobility. Further, since quantum devices are smaller in scale than micron-scale electronics, they operate faster. Quantum devices also offer greater flexibility than conventional semiconductor electronics; one double-barrier heterostructure can reproduce the functions of fifteen transistors.

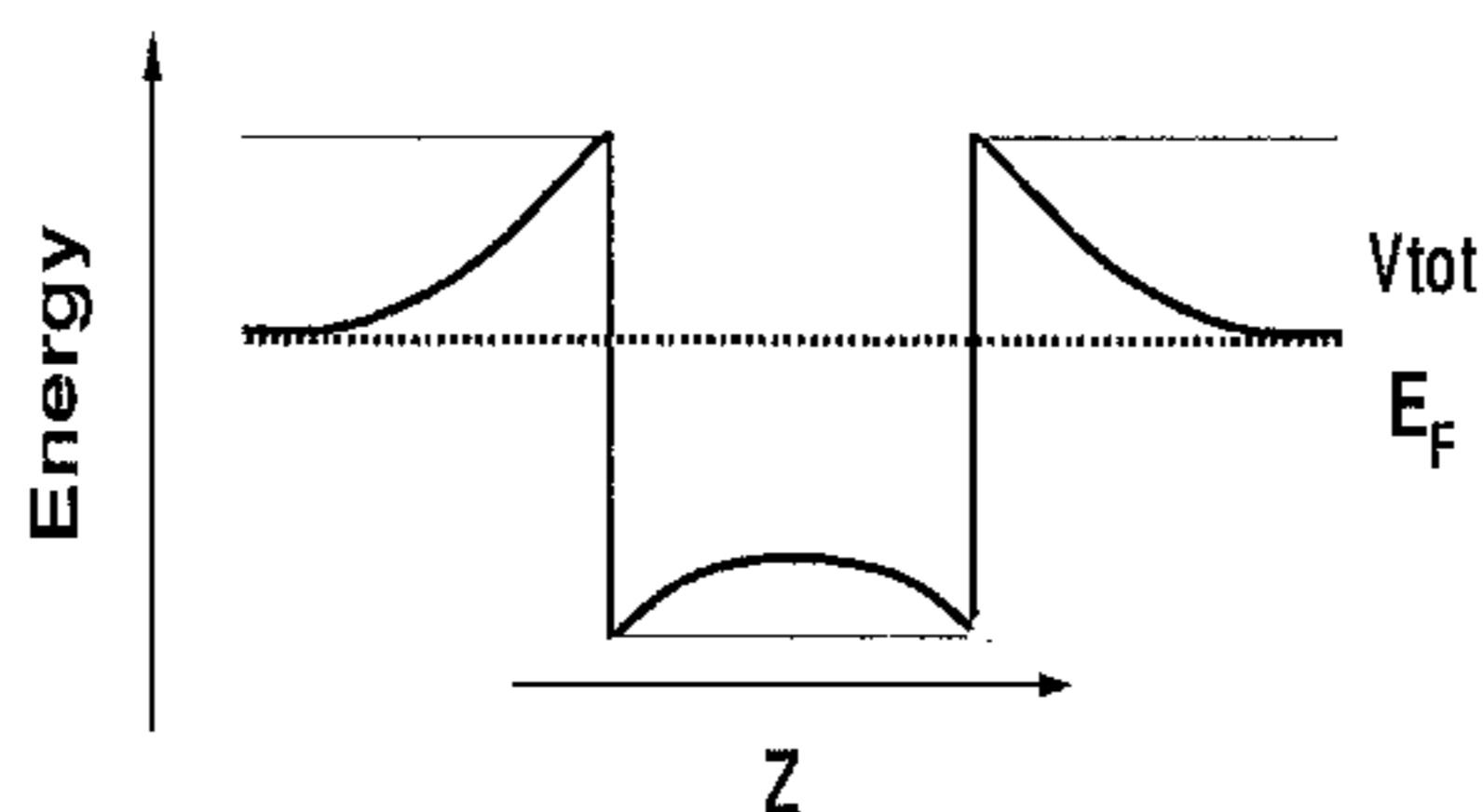
The atomic-scale construction techniques discussed above provide great control over the device geometry. The thickness of the layers can be precisely controlled. By growing material in monoatomic layers atop a semiconductor substrate, one can match crystals with different lattice constants. Semiconductor alloys with a desired bandgap can be constructed from two different materials by controlling the percentage of material of each type grown into the alloy. Lastly, the precise placement and density of donors can be controlled. These factors all affect the properties of the heterostructure.

One can also apply external magnetic or electric fields to the heterostructure. External magnetic fields can be applied perpendicular or parallel to the layers. These fields cause the electrons to orbit, thus changing their energy. Similarly, one can apply an external electric field by connecting the structure to an external voltage source, creating a quantum

electronic device. Our algorithm must efficiently and accurately solve for the energy levels of a quantum heterostructure of specified construction subject to the presence of an in-plane or perpendicular magnetic field and/or external electric field.

In an actual physical quantum well, electrons from the barriers fall into the well and become trapped. The changing charge density superimposes a new potential (see figure 3). This new potential alters the structure's intrinsic energy levels and their associated

Figure 3: Self-Consistent Quantum Well

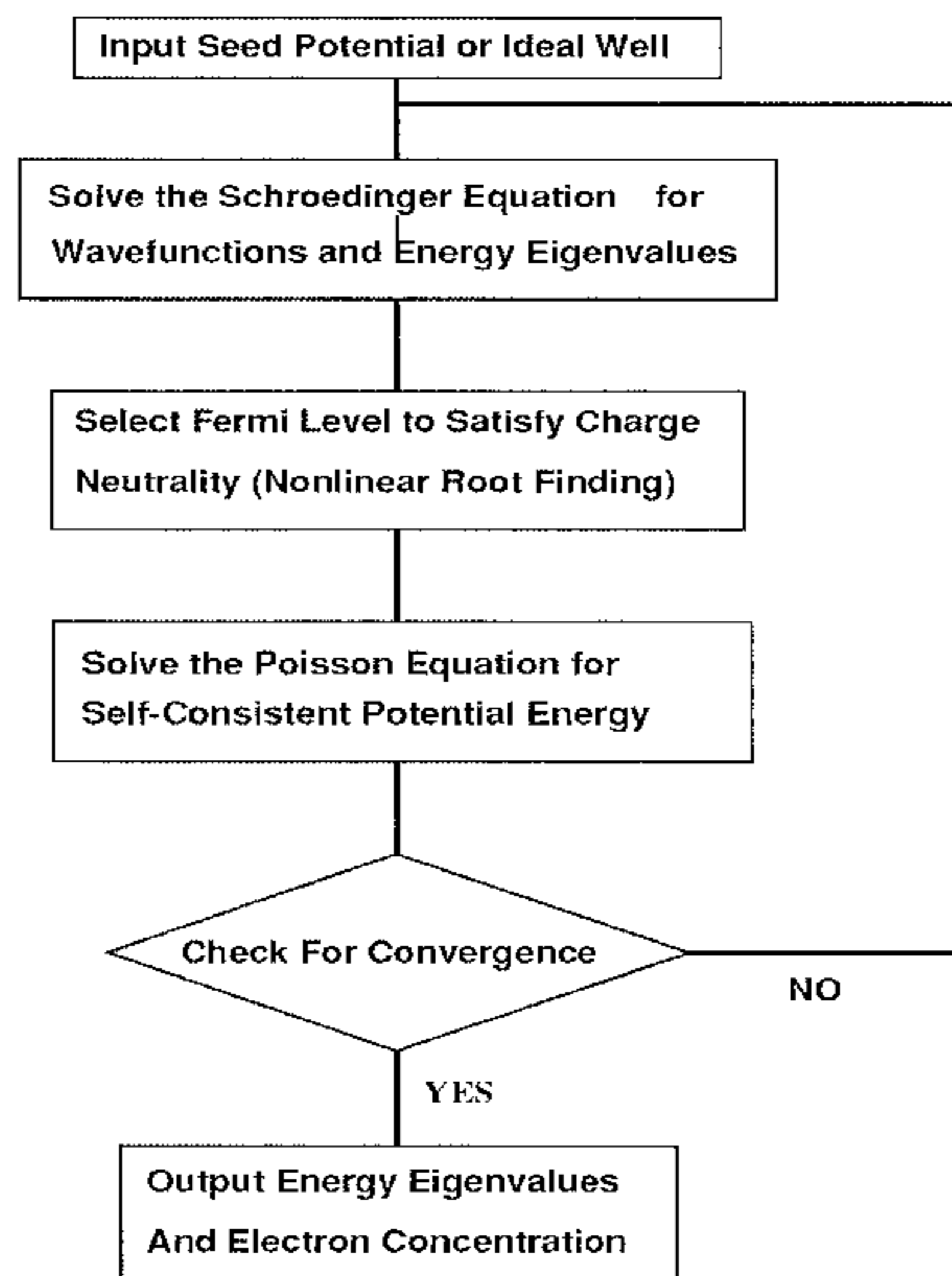


Self-consistent potential energy and Fermi level for quantum well.

wavefunctions, thus further altering the charge density. To obtain the energy levels for the physical heterostructure we must iteratively solve the Schroedinger equation for the energy eigenvalues, then solve the Poisson equation for the new total potential. Because the Poisson equation depends on the heterostructure's Fermi level, we must as an intermediate step find the Fermi level through the requirement that the heterostructure's net charge be nearly zero. We are led to a three step iterative process (see figure 4).

We first solve the Schroedinger equation for the energy eigenvalues. Next using these eigenvalues we find the Fermi level through the charge neutrality requirement. Using this

Figure 4: Iterative Self-Consistent Algorithm



Fermi level and the eigenvalues we solve Poisson's equation for the new total potential. When successive corrections to the potential become small the iteration has converged to a self-consistent solution.

To solve the Schroedinger and Poisson differential equations for the energy levels and effective potential energy, respectively, we employ the finite element technique. While finite element and boundary integral methods have been extensively employed in engineering fields, scientists have not fully embraced these exceptionally powerful numerical tools. These methods present substantial advantages in terms of accuracy and efficiency. Further, when paired with the Hermite interpolating polynomials, detailed later, finite elements naturally enforce derivative continuity. We employ the Galerkin implementation of the finite element method to solve the Poisson differential equation and in so doing explore the method's natural suitability for complex physical problems.

2 The Self-Consistency Problem

2.1 Poisson's Equation – FEM Formulation

We begin with the differential relation for Gauss' law (in CGS units)

$$\nabla \cdot \mathbf{D} = 4\pi\rho_f, \tag{1}$$

with

$$\mathbf{D} = \mathbf{E} + 4\pi\mathbf{P}(z) \tag{2}$$

where \mathbf{D} is the electric displacement, \mathbf{E} the electric field, \mathbf{P} the dielectric polarizability, and ρ the free charge. In a linear dielectric with susceptibility $\chi(z)$ such that $\mathbf{P} = \chi(z)\mathbf{E}$,

$$\mathbf{D} = (1 + 4\pi\chi(z))\mathbf{E} \tag{3}$$

or, introducing the dielectric constant $\epsilon(z)$ (which may vary along the growth direction z),

$$\mathbf{D} = \epsilon(z)\mathbf{E}, \tag{4}$$

Substituting 4 into 1, we have

$$\nabla \cdot (\epsilon(z)\mathbf{E}) = 4\pi\rho. \tag{5}$$

We can write the electric field as the gradient of a scalar potential ϕ^1 , so that

$$\mathbf{E} = -\nabla\phi. \quad (6)$$

If we define the potential *energy* $V = -|e|\phi$, which we will measure in electron-volts (eV), we have (substituting into 5)

$$+\nabla \cdot [\epsilon(z)\nabla V] = +4\pi|e|\rho. \quad (7)$$

In our one-dimensional heterostructure, $\nabla = \frac{d}{dz}$. For convenience we measure heterostructure dimensions in Angstroms. We denote Angstrom dimensions by \tilde{z} , where $z = 10^{-8}\tilde{z}$. Then $\nabla = \frac{d}{dz} \frac{d\tilde{z}}{dz} = 10^8 \tilde{\nabla}$. We change to $\tilde{\nabla}$ and scale the right hand side by $10^{-16} \text{ cm}^2 / \text{Å}^2$. We further define the quantity

$$\bar{\rho}(\tilde{z}) \equiv 4\pi|e|10^{-16}\rho(\tilde{z}). \quad (8)$$

Superposition allows us to separate $\tilde{\nabla}^2 V = \bar{\rho}/\epsilon$ and solve for the self-consistent energy independently of the intrinsic material bandgap profile V_o or any externally applied V_e . Hereafter V and $\bar{\rho}$ refer to the self-consistent potential energy and charge.

We can multiply both sides of (7) by V and integrate over the heterostructure limits $[a, b]$ and then integrate the left hand side by parts to obtain

$$V\epsilon(\tilde{z})\nabla V \Big|_a^b - \int_a^b \nabla V \cdot (\epsilon(\tilde{z})\nabla V) d\tilde{z} = \int_a^b V\bar{\rho}(\tilde{z})d\tilde{z}. \quad (9)$$

¹The scalar potential ϕ is not related to the interpolating polynomials $\phi_i(\xi)$ described in Sec. 4.

Since $\nabla V = |e|\mathbf{E}$ and the self-consistent $\mathbf{E} = 0$ at a and b for a quantum well, the surface term vanishes. For a superlattice, a and b are the same point by virtue of periodicity, and again the surface term vanishes. We now discretize our integration into integrals over each element and approximate V using the Hermite polynomial approximation $V \cong V_i \Phi_i$ discussed in Sec. 4 to obtain

$$-\epsilon \int_{-1}^1 \Phi'_i V_j \Phi'_j \frac{d\tilde{z}}{d\xi} d\xi = \int_{-1}^1 \Phi_i \bar{\rho}(\tilde{z}) \frac{d\tilde{z}}{d\xi} d\xi. \quad (10)$$

where we have taken ϵ to be constant over each element and canceled an extraneous factor of V_j from both sides, and have changed the integration variable to the local element coordinate ξ . In each element we perform the Gaussian quadrature integration [11]

$$\int_{-1}^1 f(x(\xi)) d\xi \cong \sum_{k=1}^N w_k f(\xi_k) \quad (11)$$

where N is here the number of Gauss points ξ_k , and w_k is the weight associated with each point. Since V_j is not a function of ξ we can factor it out of the sum and write

$$-\left[\sum_{k=1}^N w_k \epsilon \Phi'_i \Phi'_j \frac{d\tilde{z}}{d\xi} \right] V_j = \left[\sum_{k=1}^N \Phi_i \bar{\rho}(\tilde{z}) \frac{d\tilde{z}}{d\xi} \right] \quad (12)$$

and associate the bracketed quantities with the element matrices m_{ij} and r_i , respectively. To find the total integral over the heterostructure we must construct the global matrices M_{IJ} and R_I from the element matrices through matrix overlays. We will next proceed to develop the overlays from the continuity relations.

2.2 Continuity Conditions

Because the $\xi = 1$ node of one element is the same point as the $\xi = -1$ point of the next, we must overlay the matrices to impose continuity on the finite element discretization. Our continuity conditions require that at an element interface

$$V_L = V_R \quad (13)$$

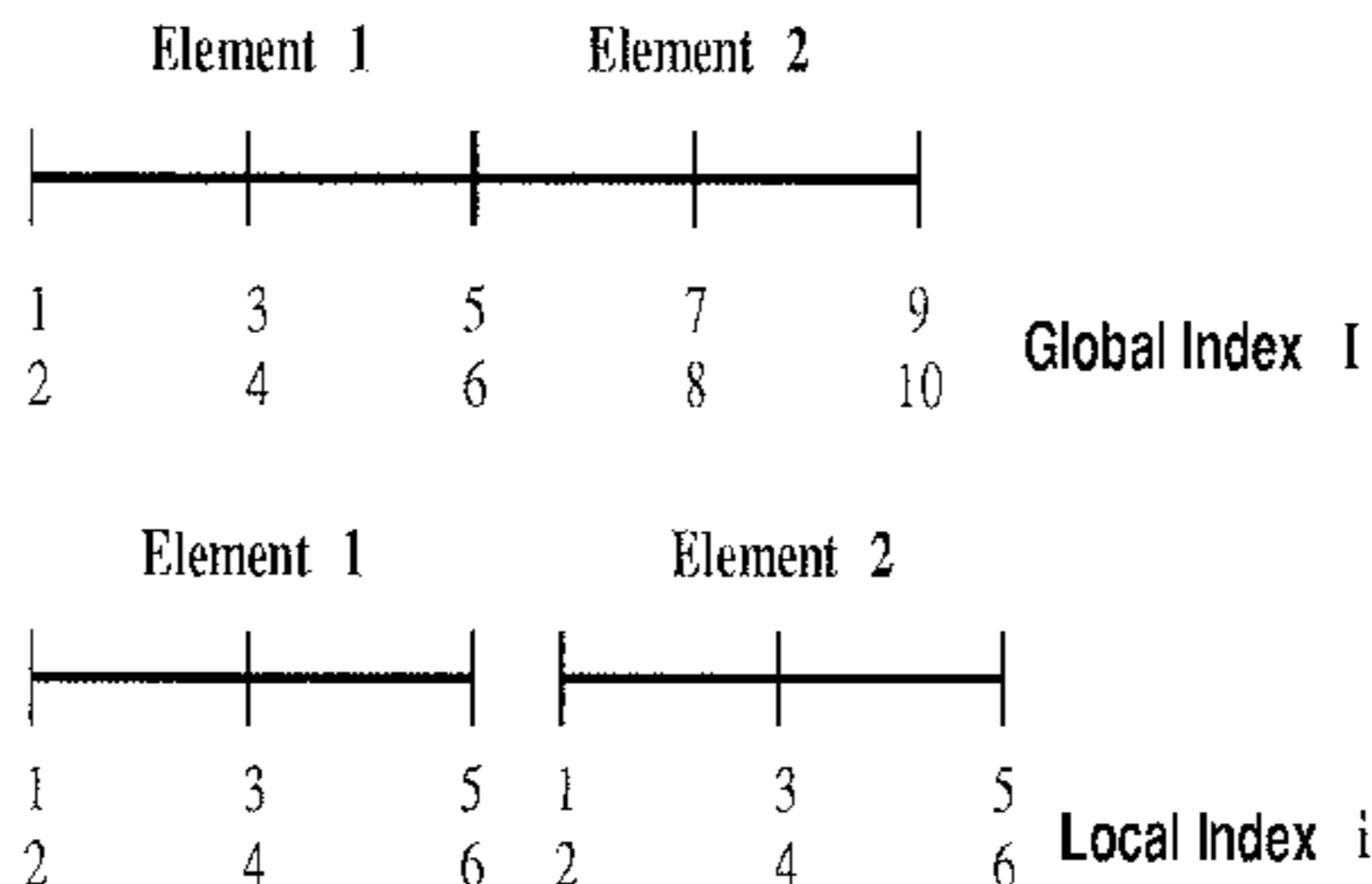
and

$$\epsilon_L V'_L = \epsilon_R V'_R. \quad (14)$$

Eq. (13) represents continuity of the potential ϕ since $V = -|e|\phi$. Eq. (14) expresses continuity of the displacement field \mathbf{D} , since $\epsilon V' = \epsilon \nabla V = |e|\epsilon \mathbf{E} = |e|\mathbf{D}$. Continuity of \mathbf{D} can be shown by considering a Gaussian pillbox that straddles a layer interface. As the pillbox becomes infinitesimal, only D_n , the component of \mathbf{D} normal to the pillbox, contributes; the net flux through the surface becomes the difference between D_n in the first material and D_n in the second. The integral form of Gauss' law, Eq. (4), states that the net flux of \mathbf{D} through a closed surface is proportional to the free charge enclosed. Since the enclosed free charge goes to zero as the volume enclosed by the pillbox becomes infinitesimal, D_n is continuous across layer interfaces.

We consider two adjacent elements (see figure 5), whose element matrices we call m_L and m_R and recall that in each we have made the approximation $V \cong V_i \Phi_i$ discussed in Sec. 4. Each element has its own local index i , which runs from 1 to 6 with the odd number indices corresponding to nodal points storing the function's value and the even index numbers

Figure 5: Local and Global Element Indices



corresponding to the derivative nodal points. To avoid confusion we rename the local index to be i' in the right element.

Eq. (13) implies that the $i = 5$ nodal point of V in the left element and the $i' = 1$ nodal point of V in the right element are the same. Thus the $i = 1$ row of m_L and the $i' = 5$ row of m_R are the same. We decide to express our equations in terms of the left element nodal points. We add the first row of m_R to the fifth row of m_L and add the first row of r_R to the last row of r_L .

Eq. (14) requires that replace the right derivative point $V_{i=6}$ by ϵ_L/ϵ_R times the left derivative point $V_{i'=2}$. This corresponds to scaling the second row of r_R and adding it to the last row of r_L . Since m_R involves $\Phi'_{i'}$ and $\Phi'_{j'}$, we must scale its second row and column (corresponding to the i' and j' indices, respectively) before adding them to m_L .

These overlays produce banded block-diagonal matrices, and we solve Poisson's equation in the finite-element formulation

$$- M_{IJ}V_J = R_I, \tag{15}$$

where I and J are global indices running over the total overlaid matrix M , not to be confused

with the local indices i and j which run over the 6×6 element submatrices m_{ij} .

2.3 Source Terms in Poisson's Equation

In the final finite element formulation of Poisson's equation given by Eq. (15), we see that the right hand side is given by R_I , which we construct by overlaying the element vectors

$$r_i = \left[\sum_{k=1}^N \bar{\rho}(\tilde{z}) \Phi_i \frac{d\tilde{z}}{d\xi} \right]. \quad (16)$$

We can separate $\bar{\rho}(\tilde{z})$ into $\bar{\rho}_e(\tilde{z})$ and $\bar{\rho}_d(\tilde{z})$, where $\bar{\rho}_d(\tilde{z})$ is the ionized donor charge density and $\bar{\rho}_e(\tilde{z})$ is the electron contribution. We proceed to find the electron and donor charge densities and their associated contribution to the finite element formulation of Poisson's equation.

The negative charge density is given by

$$\rho_e = -|e|n_e(z), \quad (17)$$

where $n_e(z)$, the number density of electrons, is given by

$$n_e(z) = \sum_{n_x, n_y, n_z, n_s} |\Psi(x, y, z, t)|^2 f(E) \quad (18)$$

where the sum extends over all allowed quantum numbers. Here $f(E)$ is the Fermi distribution function

$$f(E) = \frac{1}{e^{(E-E_F)/k_B T} + 1} \quad (19)$$

where E_F is the Fermi energy, k_B the Boltzmann constant, and T the temperature in Kelvin.

Thus the number density of electrons as a function of position is the probability that an

electron with a certain set of quantum numbers will be at that position, multiplied by the probability that a free state at that energy will exist, summed over all allowed sets of quantum numbers. The sum over the spin quantum number n_s just introduces a factor of 2. The sum over n_z is a sum over heterostructure eigenstates below the Fermi level; we rename it as a sum over i . In the x and y directions, electron states are continuous. We transform the sums over n_x, n_y to integrals in phase space through the application of the periodic boundary conditions

$$k_{x,y} = \frac{2\pi n_{x,y}}{L} \quad (20)$$

and use separation of variables to write

$$\Psi(x, y, z, t) = \frac{\psi(z)e^{ik_x x} e^{ik_y y} e^{iEt/\hbar}}{(\sqrt{L})^2}, \quad (21)$$

where we have assumed the normalization

$$\int |\psi(z)|^2 dz = 1 \quad (22)$$

in CGS units, to obtain

$$n_e(z) = 2 \sum_i \left(\frac{L}{2\pi}\right)^2 \iint \frac{|\psi(x)|^2}{L^2} f(E) dk_x dk_y \quad (23)$$

Since $E = \frac{\hbar^2}{2m^*}(k_x^2 + k_y^2 + k_z^2)$, where m^* is the electron effective mass in the planar layer, we define

$$k_{\perp} \equiv \sqrt{k_x^2 + k_y^2} \quad (24)$$

so that

$$E = E_{\perp} + E_i. \quad (25)$$

Performing the polar transformation

$$\int_0^{\infty} \int_0^{\infty} dk_x dk_y = \int_0^{2\pi} \int_0^{\infty} k_{\perp} dk_{\perp} d\theta \quad (26)$$

and doing the integration over θ , we have that

$$n_e = \sum_i \frac{|\psi_i(z)|^2}{\pi} \int_0^{\infty} \frac{1}{e^{(E_{\perp} + E_i - E_F)/k_B T} + 1} k_{\perp} dk_{\perp}. \quad (27)$$

Using the relation $d(k_{\perp}^2) = 2k_{\perp} dk_{\perp} = \frac{2m^*}{\hbar^2} dE_{\perp}$, we have that

$$n_e(z) = \sum_i \frac{|\psi_i(z)|^2}{\pi} \int_0^{\infty} \frac{m^*}{\hbar^2} \left(\frac{k_B T}{k_B T} \right) \left(\frac{e^{-E_{\perp}/k_B T}}{e^{(E_i - E_F)/k_B T} + e^{-E_{\perp}/k_B T}} \right) dE_{\perp}. \quad (28)$$

Introducing the temporary integration variable $x = \frac{E_{\perp}}{k_B T}$, we see that

$$n_e(z) = \sum_i |\psi_i(z)|^2 \frac{m^* k_B T}{\pi \hbar^2} \int_0^{\infty} \left(-\frac{d}{dx} \ln \left(e^{(E_i - E_F)/k_B T} + e^{-x} \right) \right) dx. \quad (29)$$

Evaluating at the limits $(0, \infty)$ we obtain

$$n_e(z) = \sum_i |\psi_i(z)|^2 \frac{m^* k_B T}{\pi \hbar^2} \ln \left(1 + e^{(E_F - E_i)/k_B T} \right), \quad (30)$$

which is valid for any finite temperature.

In the $T = 0$ limit, $f(E)$ becomes the step function $\theta(E)$, defined as

$$\theta(x) = \begin{cases} 0 & x < 0 \\ 0.5 & x = 0 \\ 1 & x > 0 \end{cases} \quad (31)$$

and Eq. (23) becomes

$$n_e(z) = 2 \sum_i \left(\frac{L}{2\pi} \right)^2 2\pi \int_0^\infty \frac{|\psi_i(z)|^2}{L^2} \theta(E_F - E_\perp - E_i) dk_x dk_y \quad (32)$$

$$= \sum_i \frac{m^*}{\pi \hbar^2} |\psi_i(z)|^2 E_\perp \Big|_0^{E_F - E_i} \quad (33)$$

$$= \sum_i \frac{m^*}{\pi \hbar^2} |\psi_i(z)|^2 (E_F - E_i) \quad (34)$$

Then using $\rho_e = -|e|n_e$ we can write

$$\bar{\rho}_e(\tilde{z}) = -10^{-16} \left(\frac{4\pi|e|^2}{\hbar c} \hbar c \right) \left(\frac{m^*}{m_0} \right) \left(\frac{m_0}{\pi \hbar^2} \right) \sum_i |\psi_i(z)|^2 (E_F - E_i), \quad (35)$$

where we have introduced the energy $\hbar c$ and the electron rest mass m_0 to transform to convenient constants. We measure $\psi(\tilde{z})$ in Angstroms, converting $\psi(\tilde{z})$ to cm through the relation $|\psi_i(z)|^2 = 10^8 |\psi_i(\tilde{z})|^2$. Collecting the constants in eV and CGS units, we find

$$\bar{\rho}_e(\tilde{z}) = -7.5580471 \left(\frac{m^*}{m_0} \right) \sum_i |\psi_i(\tilde{z})|^2 (E_F - E_i). \quad (36)$$

The positive charge is more easily obtained as

$$\rho_d(\tilde{z}) = +|e|n_D(\tilde{z})\theta(V_{tot}(\tilde{z}) - E_d - E_F), \quad (37)$$

which states that donors with energy $V_{tot}(\tilde{z})$ of at least E_d above the Fermi level contribute the local donor density $n_d(\tilde{z})$. Thus

$$\bar{\rho}_d(\tilde{z}) = -10^{-16} \left(\frac{4\pi|e|^2}{2a_0} 2a_0 \right) n_d \theta(V_{tot}(\tilde{z}) - E_d - E_F), \quad (38)$$

where we again transform to convenient constants, which when evaluated yield the final form

$$\bar{\rho}_d(\tilde{z}) = 1.8093083 \times 10^{-6} \left(\frac{n_d}{10^{16}} \right) \theta(V_{tot}(\tilde{z}) - E_d - E_F). \quad (39)$$

2.4 Fermi Level Solution

To evaluate the Fermi level we require that the total charge over the heterostructure be nearly zero; that is,

$$\int_a^b \rho_e(\tilde{z})d\tilde{z} \cong \int_a^b \rho_d(\tilde{z})d\tilde{z} \quad (40)$$

or, substituting Eq. (34) and (37),

$$\int_a^b n_D(\tilde{z}) \theta(V_{tot}(\tilde{z}) - E_d - E_F) d\tilde{z} \cong \int_a^b \frac{m^*(\tilde{z})}{\pi \hbar^2} \sum_i |\psi(\tilde{z})|^2 (E_F - E_i) d\tilde{z} \quad (41)$$

where we have canceled off factors of $|e|$ from each side. This equation is nonlinear and must itself be solved iteratively. We must therefore impose limits on E_F . We require that the Fermi level lie above the first bound state and below the top of the well. A further complication arises because the region where donors contribute, where $(V_{tot}(\tilde{z}) - E_d - E_F) > 0$, does not coincide with the element boundaries. To integrate accurately we keep track of ionization regions within each element and integrate over each region by Gaussian quadrature. These integration regions are found by using Brent's algorithm [3] to find the roots of $V_{tot}(\tilde{z}) - E_d - E_F = 0$. The Fermi level solution algorithm is thus a nonlinear root finder solving the equation

$$\int_a^b \rho dz = 0. \quad (42)$$

The Fermi level nonlinear root finder itself incorporates a Brent's algorithm root finder. On every iteration through the Fermi level solution, we integrate the negative charge over each element. Within an element we find the ionization regions with Brent's method and integrate over each region. The Fermi level is adjusted towards charge neutrality and we iterate again.

3 FEM Boundary Conditions

In the development of Eq. (10) from Eq. (9), we discarded the surface term by arguing that the electric field vanished at the heterostructure boundaries. While this condition is true, we must apply boundary conditions to the finite element implementation to fix our self-consistent energy V . For this purpose we will find retention of the surface terms an advantage in terms of insight and generality. We proceed, then, to derive the application of boundary conditions to our finite-element formulation of the self-consistency problem.

From Eq. (9) we see that with the use of Eq. (8) we can write

$$V\epsilon(\tilde{z})\tilde{\nabla}V\Big|_a^b - \int_a^b \tilde{\nabla}V \cdot (\epsilon(\tilde{z})\tilde{\nabla}V) d\tilde{z} = \int_a^b V\bar{\rho}(\tilde{z})d\tilde{z}. \quad (43)$$

Within each element we utilize the Hermite polynomial approximation $V \cong V_i\Phi_i$ from Sec. 4 and cancel an extraneous factor of V_i , so that

$$-\epsilon \int_{-1}^1 \Phi'_i V_j \Phi'_j \frac{d\tilde{z}}{d\xi} d\xi = \int_{-1}^1 \Phi_i \bar{\rho}(\tilde{z}) \frac{d\tilde{z}}{d\xi} d\xi \quad (44)$$

while the global integrals, which can be broken down into sums of the integrals over each element, have the form

$$-\int_a^b \epsilon(\tilde{z})\Phi'_I V_J \Phi'_J d\tilde{z} = \int_a^b \Phi_I \bar{\rho}(\tilde{z}) d\tilde{z} - \epsilon \Phi_I V_J \Phi'_J \Big|_a^b. \quad (45)$$

Here we have carefully distinguished between the global indices I and J and the local indices i and j . This last term in (45) appears only as a global quantity, since it is evaluated only

at the heterostructure bounds. Following Eqs. (11) and (12) we can do the integrals by Gaussian quadrature in each element, define element submatrices m_{ij} and r_i , and overlay the submatrices according to the boundary conditions (13) and (14). We recover the previous finite element formulation (15), this time keeping the global surface terms, so that

$$-M_{IJ}V_J = R_I - \epsilon\Phi_I V_J \phi'_J \Big|_a^b. \quad (46)$$

The nodal vector V_J alternately specifies a function or derivative nodal value, depending on whether J is even or odd, respectively. The surface term fixes the value of $V = V_I \Phi_I$ at a and b and thus modifies the $I = 1$ and $I = n - 1$ rows (where n is the number of equations). The surface term also specifies $\tilde{\nabla}V = V_J \Phi'_J$ at a and b . Effectively this sets the first and last derivative terms, where $J = 2$ and $J = n$ at a and b , respectively. We then have

$$-M_{IJ}V_J = R_I + \epsilon V'_{I=1, J=2} - \epsilon V'_{I=n-1, J=n}. \quad (47)$$

We can show the boundary conditions more clearly in matrix form as

$$\begin{bmatrix} M_{11} & \cdots & M_{1n} \\ \vdots & & \vdots \\ \vdots & & \vdots \\ M_{n1} & \cdots & M_{nn} \end{bmatrix} \begin{bmatrix} V_1 \\ V_2 \\ \vdots \\ V_{n-1} \\ V_n \end{bmatrix} = \begin{bmatrix} R_1 + \epsilon V_2 \\ R_2 \\ \vdots \\ R_{n-1} - \epsilon V_n \\ R_n \end{bmatrix} \quad (48)$$

where M is actually block-diagonal, but we have drawn it as a full matrix for illustrative

purposes, and M_{IJ} is the sum of the submatrices

$$m_{ij} = \sum_{k=1}^N w_k \epsilon \Phi'_i \Phi'_j \frac{d\bar{z}}{d\xi} \quad (49)$$

with suitable overlays to enforce continuity between adjacent elements.

A second-order differential equation requires two boundary conditions. We are left with three possibilities for specifying these boundary conditions. We can specify i) V at a and b , ii) V at one end and V' at the other, or iii) V and V' at the same point ². For a known V_i , we can make the i 'th matrix equation into the trivial equation $V_i = V_{bc}$ by replacing R_i with V_{bc} , setting $M_{ii} = 1$, and zeroing all elements of the i 'th row except M_{ii} . Immediately we recognize the ability to eliminate the surface terms entirely by specifying V_a and V_b , since

$$\begin{bmatrix} 1 & 0 & \cdots & \cdots & 0 \\ M_{21} & M_{22} & \cdots & \cdots & M_{2n} \\ \vdots & & & & \vdots \\ 0 & \cdots & 0 & 1 & 0 \\ M_{n1} & \cdots & \cdots & \cdots & M_{nn} \end{bmatrix} \begin{bmatrix} V_1 \\ V_2 \\ \vdots \\ V_{n-1} \\ V_n \end{bmatrix} = \begin{bmatrix} V_a \\ R_2 \\ \vdots \\ V_b \\ R_n \end{bmatrix}. \quad (50)$$

If we specify V at a and V' at b , we eliminate one surface term and the other has been

²We must specify V at some point; specifying derivatives alone does not uniquely determine the function.

specified, so we add it to the right hand side to obtain

$$\begin{bmatrix} 1 & 0 & \cdots & \cdots & 0 \\ M_{21} & M_{22} & \cdots & \cdots & M_{2n} \\ \vdots & & & & \vdots \\ M_{n-1,1} & \cdots & \cdots & \cdots & M_{n-1,n} \\ 0 & \cdots & 0 & 1 & 0 \end{bmatrix} \begin{bmatrix} V_1 \\ V_2 \\ \vdots \\ V_{n-1} \\ V_n \end{bmatrix} = \begin{bmatrix} V_a \\ R_2 \\ \vdots \\ R_{n-1} - \epsilon V_n \\ R_n \end{bmatrix} \quad (51)$$

Specifying both V and V' at a is the most troublesome, since one surface term is then an unknown quantity and we must therefore bring it to the left hand side by adding it to $M_{n-1,n}$. We then have

$$\begin{bmatrix} 1 & 0 & \cdots & \cdots & 0 \\ 0 & 1 & 0 & \cdots & 0 \\ M_{31} & M_{32} & M_{33} & \cdots & M_{3n} \\ \vdots & & & & \vdots \\ M_{n-1,1} & \cdots & \cdots & M_{n-1,n-1} & M_{n-1,n} + \epsilon \\ M_{n1} & \cdots & \cdots & \cdots & M_{nn} \end{bmatrix} \begin{bmatrix} V_1 \\ V_2 \\ \vdots \\ V_{n-1} \\ V_n \end{bmatrix} = \begin{bmatrix} V_a \\ V_b \\ \vdots \\ R_{n-1} \\ R_n \end{bmatrix}. \quad (52)$$

This boundary condition, while conceptually no different from the previous conditions, is in practice much harder to implement. Because it perturbs the left hand matrix M , one can no longer factor M and use its initial solution in successive iterations. Further, since it adds derivative information to a function row, the equations swiftly become ill-conditioned and the solution loses accuracy. To solve for the self-consistent energy, we employ the second

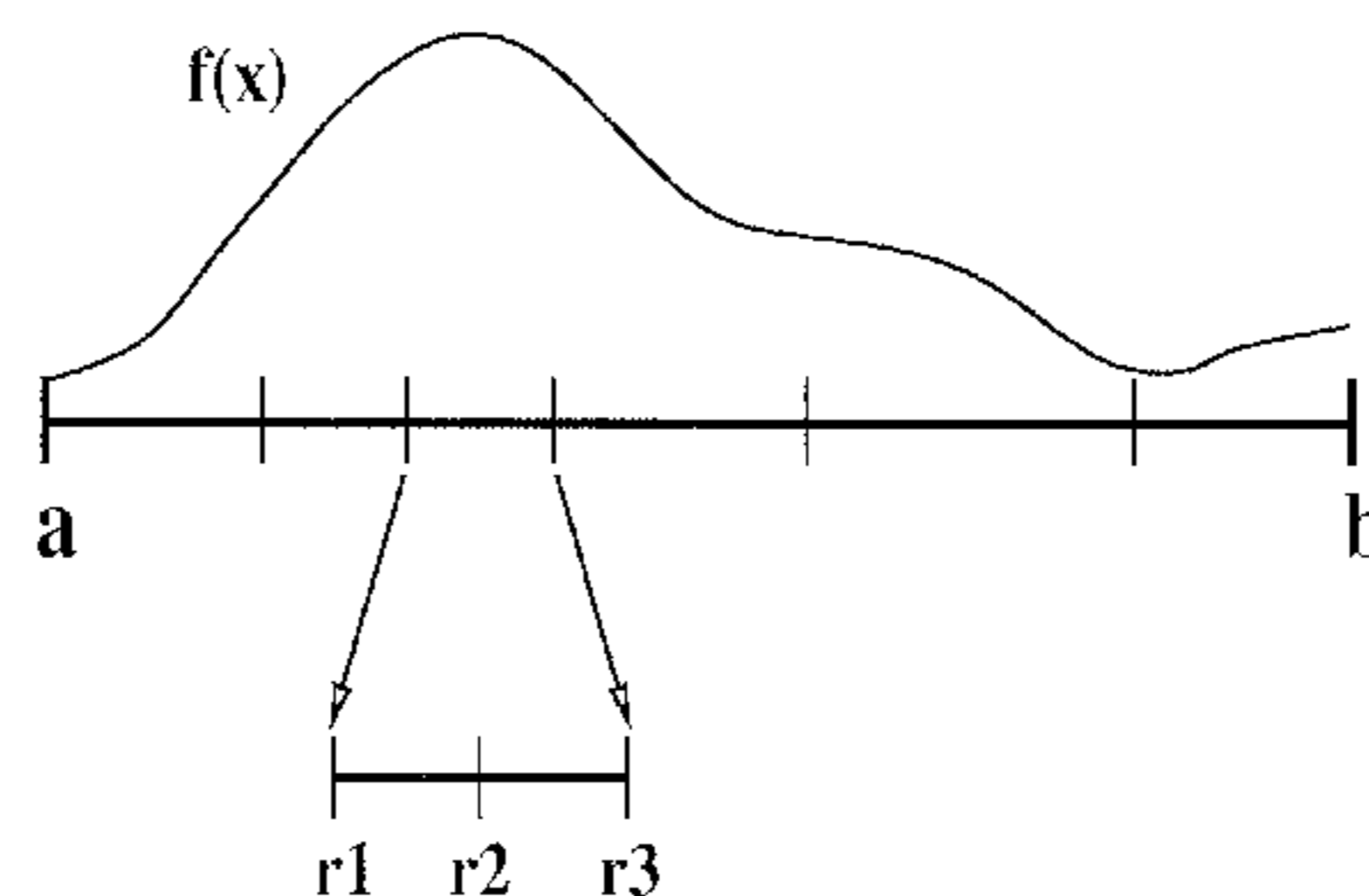
type of boundary condition discussed by specifying V at a and setting V' at b to 0.

4 The Hermite Interpolating Polynomials

Traditional series approximation methods such as Fourier and Taylor series approximate a function by its expansion in terms of orthonormal basis functions. Such methods cannot easily handle discontinuous functions because any local fitting error introduces error over the entire set of basis functions. Approximating discontinuous functions with traditional methods requires that large sets of orthogonal functions be constructed. We instead employ the finite element method with Hermite interpolation. The finite element method is superior because it approximates the function by a separate interpolating polynomial within each element, so fitting errors are localized. We improve on simple linear finite elements by the use of the Hermite interpolating functions, which maintain continuity of the function *and its derivative* throughout the entire region of interest. Maintaining derivative continuity provides substantial advantage in the calculation of relevant physical quantities.

We consider the approximation of a function $f(z)$ and its derivative $f'(z)$ over an element $[a, b]$ (see figure 6). The values of the function and derivative are known at nodal points within

Figure 6: Finite Element Approximation



the element. In our implementation the nodal points are the center and ends of the element.

We first rescale the range in terms of a local variable $\xi(z)$ with range $[-1, 1]$ through the mapping

$$z = \frac{a+b}{2} + \frac{b-a}{2}\xi \quad (53)$$

Each order of the derivative defines a *degree of freedom*; we use the 0'th and 1'st derivatives, or two degrees of freedom. To satisfy the requirement that the interpolation be exact for the function and its derivative at the nodal points we use a separate polynomial for each combination of derivative and nodal point. We define $\phi(\xi)$ and $\bar{\phi}(\xi)$ so

$$\phi_i(\xi_i) = 1 \quad \phi_i(\xi_j) = 0 \quad \phi'_i(\xi_i) = 0 \quad (54)$$

$$\bar{\phi}'_i(\xi_i) = 1 \quad \bar{\phi}'_i(\xi_j) = 0 \quad \bar{\phi}_i(\xi_i) = 0 \quad (55)$$

where $\xi_i = -1, 0, 1$ for $i = 1, 2, 3$, and $j \neq i$. Then the approximation

$$f(\xi) \cong \sum_{i=1}^3 f_i \phi_i(\xi) + \sum_{i=1}^3 f'_i \bar{\phi}_i(\xi) \frac{dz}{d\xi} \quad (56)$$

gives the exact values f_n at the nodes. Here f_n and f'_n are the (constant) nodal values³ of the function and its derivative, respectively, and may in general be complex. The factor of $dz/d\xi$ insures that

$$f'(\xi) \cong \sum_{i=1}^3 f_i \phi'_i(\xi) \frac{d\xi}{dz} + \sum_{i=1}^3 f'_i \bar{\phi}'_i(\xi) \quad (57)$$

³Note that f'_n is here a constant, not $\frac{d}{dz} f_n$.

gives the correct values f'_n at the nodes (where $f_n = 0$). For our mapping (53),

$$\frac{dz}{d\xi} = \frac{a-b}{2} \quad (58)$$

A set of functions satisfying these properties has been identified [17]. The interpolation can be extended to higher degrees of freedom or more nodal values; procedures for both extensions have been shown elsewhere [12].

We can define the scaled interpolation vectors

$$\Phi_i = \begin{cases} \phi_i(\xi_i) & i = 1,3,5 \\ \overline{\phi_i(\xi_i)} \frac{dz}{d\xi} & i = 2,4,6 \end{cases} \quad (59)$$

$$\Phi'_i = \begin{cases} \phi_i(\xi_i) \frac{d\xi}{dz} & i = 1,3,5 \\ \overline{\phi_i(\xi_i)} & i = 2,4,6. \end{cases} \quad (60)$$

Employing the Einstein summation convention, where summation over repeated indices is implied, we can write the compact result

$$f(z) \cong f_i \Phi_i. \quad (61)$$

5 Discussion of Results

We present the self-consistent solution of a single 100 Å AlGaAs quantum well with two 5000 Å barriers and a 320 meV bandgap. This system is studied at donor densities of 10^{16} , 10^{17} , 10^{18} , and 10^{19} donors/cm³. These densities span a range from the very low to the very high. A previous project using the transfer matrix method [4], [10], mapped the lower densities but was unable to obtain convergence for the donor density of 10^{19} cm³. We consider specifically the depletion region and show that it is much larger than expected for low densities. We tabulate the relative energy level shifts associated with self-consistency and show that the separation between the first and second bound states falls as the donor density increases. This result is compared with superlattice behavior from the literature.

The algorithm can be employed to solve to a wide range of heterostructure types. We discuss some of the important structures and the variations in construction, material, donor doping, and applied E and B field that can be combined. We then discuss some of the numerical issues involved in the solution.

5.1 Depletion Region Effects

An early rough calculation during program development showed that at a donor density of 10^{16} donors per cubic centimeter the depletion region would need to extend into the micron range for all bound states in the well to be occupied. The extent of the depletion region is a substantial issue, since previous work [4] with low donor density used barriers much smaller than necessary. From the graphs of total potential (see Figs. 7, 8, 9, 10) we see that the depletion regions for a 100 Å well with a 320 meV bandgap vary significantly with donor density. We tabulate the approximate depletion regions in Table 1. The two lowest

Table 1: Approximate depletion region for 100 Å well with 320 meV bandgap

Donor Density (cm^3)	Depletion Region (Å)
10^{16}	2000
10^{17}	600
10^{18}	200
10^{19}	80

Depletion region extends to each side of well; thus the total region depleted is twice the tabulated region.

donor densities in Table 1 have one bound state contributing to the negative charge; the higher densities have two. As expected, we find the depletion region to be substantial for low donor densities. Most studies in the literature tend to consider relatively high donor densities [19], [2] or modulation doped structures [7], [14], which we will discuss later. It is therefore possible that this effect has not been given sufficient attention.

Table 2: Approximate potential energy at well center relative to well edge.

Donor Density (cm ³)	Energy Offset (meV)
10 ¹⁶	8
10 ¹⁷	23
10 ¹⁸	55
10 ¹⁹	105

Table 3: Difference between first and second energy levels for high donor densities

Donor Density (cm ³)	E ₂ -E ₁ (meV)
Ideal	97
10 ¹⁸	80
10 ¹⁹	68

5.2 Energy Level Shifting

The self-consistent solution shifts the quantum well energy levels. We find that the potential energy at the well center relative to the energy zero, which we have set at the well edge, grows dramatically with increasing donor density. This shifting is tabulated in Table 2, below. A more useful quantity is the difference between the first and second energy levels, since this can be spectroscopically observed. The lowest two donor densities have only one bound state in the well, but we can compare the energy level spacing at higher densities with those in ideal well. These values are tabulated in Table 3, below. The spacing between the first and second energy levels tends to decrease with increasing donor density. We expect this behavior, since it has been shown [7] that the first and second energy levels in a modulation doped superlattice become closer together with increasing donor density.

We note that Figs. 7, 8, 9, 10 show a Fermi level E_F which lies approximately 4 meV

below the total potential energy at the structure edge. This is to be expected, since we used a donor energy E_d of 5 meV and for a system with barriers that provide a sufficient depletion region region, $E_F + E_d > V_{edge}$ upon convergence. The donor energy of 5 meV is an appropriate value for silicon, which is frequently used as an impurity donor in GaAs structures [7] [2].

The systems studied display a high electric field in the immediate vicinity of the well edges. This effect may be significant, since a high electric field can affect GaAs, and should be further explored.

5.3 Proposed Research

The self-consistent finite element solution algorithm can be applied to a great variety of systems. We have considered the effect of changing the dopant density. One can easily vary the well width to adjust the number and spacing of energy levels. The specific doping regions can also be adjusted in a process known as modulation doping, or step-back doping [2] [7]. Modulation doping simply dopes only specific regions of the barriers, while we have here considered the barriers to be uniformly doped.

Our algorithm also allows substitution of materials with different properties, including the II-VI materials. Structures made from these materials have a band structure where the conduction band of one material can extend below the valence band of another. Coupling between energy bands is thus of great importance in these materials. Single band studies have been done of superlattice structures of layered ZnSe alternated with $\text{ZnS}_x\text{Se}_{1-x}$ doped with Li [19], and of superlattices of GaSb and InAs [9]. Because of the interband coupling effects, II-VI materials would be better treated with a multi-band approach. An eight band version of the Schroedinger solution exists and could be coupled to the self-consistent algorithm, should this become necessary. Materials in the III-V groups can be studied immediately and the single-band treatments can be immediately duplicated.

Temperatures greater than $T = 0$ can be treated by employing Eq. (30) in lieu of Eq. (36). This presents no difficulty whatsoever, since the relevant quantities are already integrated by Gaussian quadrature.

External E and B fields may be applied to the heterostructure. Externally applied E fields have been studied both theoretically [9], [6] and experimentally [16], [5]. Calculation

of external electric field effects must be done to predict the behavior of an active electronic device. The standard technique in theoretical calculations of applied electric fields is to apply a linear potential energy across the heterostructure. Our algorithm will easily support such an additional linear term. However, recent sources [20] have indicated that this may not be a sufficient approach, as hot-electron effects are significant in physical structures. These effects change the velocity distribution of the electrons and alter the applied potential, making it nonlinear. In any case, once the applied potential is truly known it becomes just another term in the potential and presents no difficulty.

Applied magnetic fields are of interest because they seemingly give rise to both the quantum Hall effect and Shubnikov-de Haas oscillations when applied to the two-dimensional electron gas in a heterostructure. Self-consistent studies of quantum wells under the presence of a strong magnetic field applied perpendicular to the heterostructure [14] show that the field changes the structure's energy states considerably. A previous project [17] adapted our finite element algorithm to solve for the energy states of conduction electrons subject to a magnetic field directed either perpendicular or parallel to the layers. We can now solve the problem of a self-consistent heterostructure with in-plane magnetic field, which is a much more difficult problem than the perpendicular field problem reported in the literature.

Different heterostructure geometries can be considered. Studies of single-barrier devices have been conducted both theoretically [18] [8] [15] and experimentally [16]. These devices are of interest because they allow for an effectively one-dimensional electron distribution. Double well and double barrier heterostructures and asymmetric wells hold great promise, as do multi-layer superlattices, since they evidence non-ohmic characteristics and can be

used to construct sophisticated, flexible devices. Our algorithm should be able to solve for the self-consistent properties of these types of structures, subject to all the variations detailed above. One difficulty would be the construction of a suitable seed potential for each radically different geometry. However, our solution has demonstrated the ability to begin iterating from an ideal potential, for low donor densities. Suitable seed potentials might be constructed by beginning with an ideal structure at low donor density; these potentials could then serve as a starting point for a high-density solution.

Finally, electron-electron interactions (known as many-body, exchange, or correlation effects) are not taken into account. Studies have considered these effects [1] but found them to be small (on the order of 1 meV). Their incorporation would be relatively straightforward and may be considered, since these effects may become non-negligible at high donor densities.

5.4 Numerical Issues

A numerical solution of this scale presents numerous difficult issues. We find that special care is required in the elimination of quasi-bound states. We additionally find that filtering the solution improves its stability greatly. The convergence rate is critical and merits special consideration. Since these issues are rarely addressed in the literature, we will consider each briefly here.

At the edges of the structure, the self-consistent potential is flat. A miniband of quasi-bound states [13] forms immediately above the self-consistent potential energy edge, as the upward-sloping potential energy curve provides an effective barrier. This miniband has been observed by others [1] but not explicitly discussed. These states present difficulties in calculation. While they are valid eigenstates, they are not bound; ie. their wavefunctions are not localized within the well. Care must be taken to see that only true bound states contribute, lest the self-consistent potential energy solution inherit the asymmetry from the quasi-bound states' wavefunctions.

The self-consistent potential energy emerging from Poisson's equation is almost completely flat at the well edges, as required by the boundary conditions and the physics. However, since the finite element method only truly solves for the nodal points and approximates in between them, a close look will show that the solution has small rises and dips between the nodal points. These small dips introduce noise and instability into the iterative process. We could control them by using extra elements, but it is computationally more efficient to filter the solution, since this makes the matrices no bigger. We filter our solution by insisting that all points below the edge potential energy be set to the edge potential energy value and

that their derivative be set to 0. This filtering is not strictly necessary; the solution will converge without it, but will converge more slowly and less smoothly.

Convergence must be carefully managed. Since the initial solution is very extreme, we apply a fraction of it and allow the system to damp down. This technique is known as cautious convergence [8]. However, we must increase the convergence factor when the solution is on track to convergence, to speed the algorithm. We thus employ adaptive cautious convergence. Our convergence is deliberately retarded to promote stability. Even so, our algorithm is quite efficient. With 25 elements and a donor density of 10^{19} donors/cm³ the algorithm converges in 36 steps. As the donor density decreases the solution takes longer, until at 10^{16} donors/cm³ 150 iterations are required for convergence. Run times are less than an hour on a DecStation 3100 workstation. The efficiency comes from the inherent efficiency of the finite element technique. As detailed elsewhere [12], finite elements provide substantial advantage in terms of accuracy as well.

Figure 7: Quantum Well, Donor Density 10^{16}

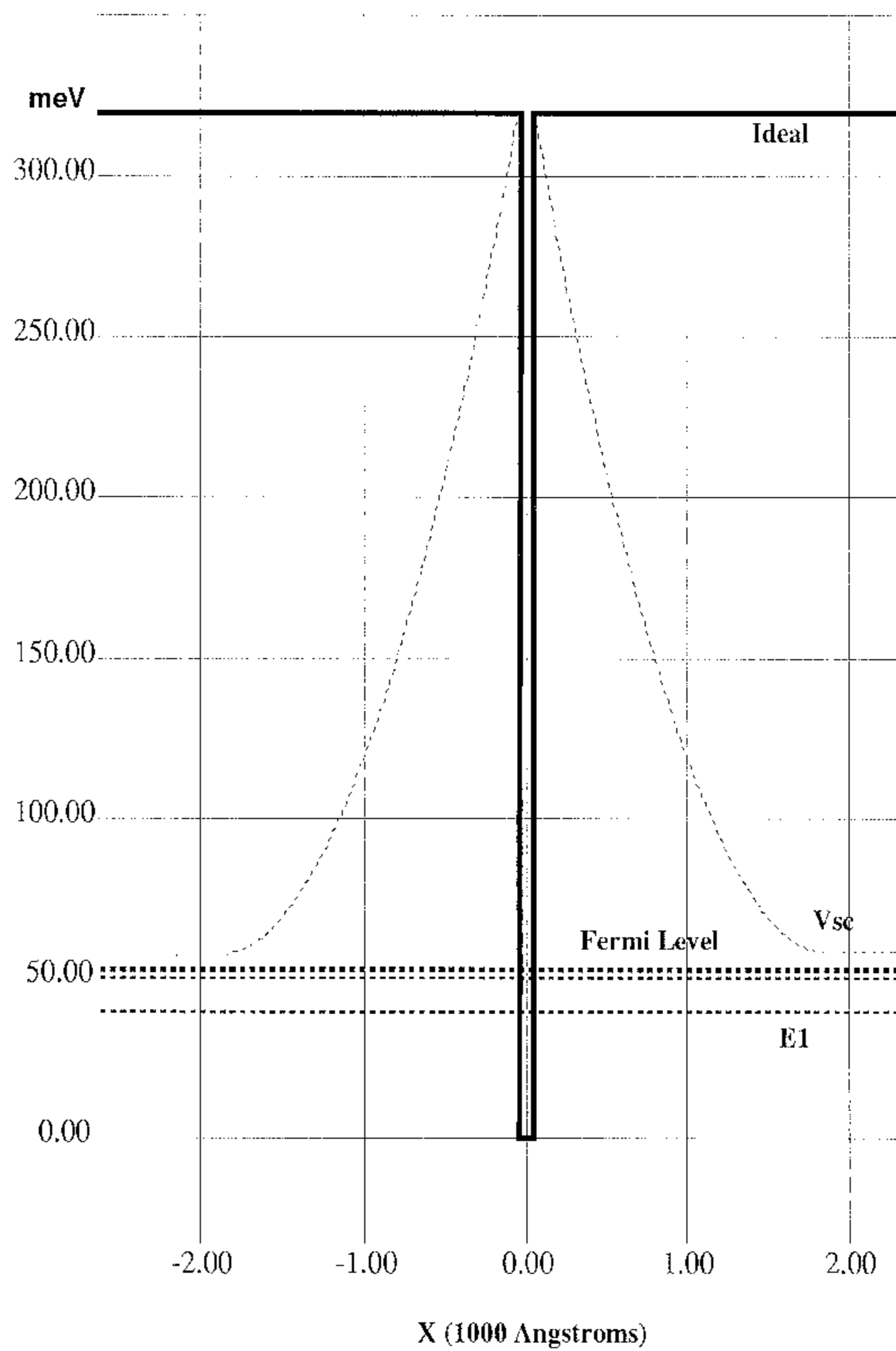


Figure 8: Quantum Well, Donor Density 10^{17}

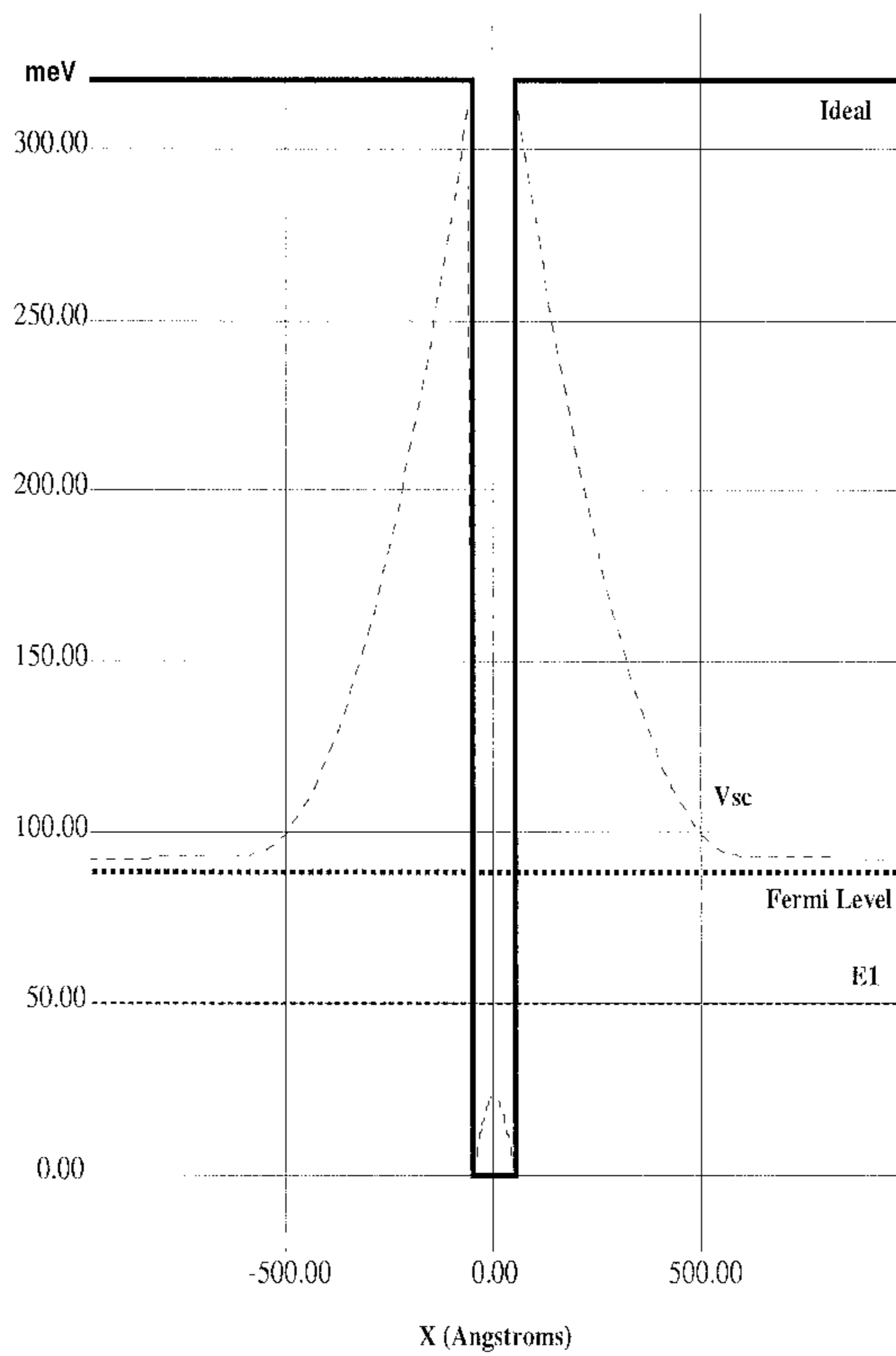


Figure 9: Quantum Well, Donor Density 10^{18}

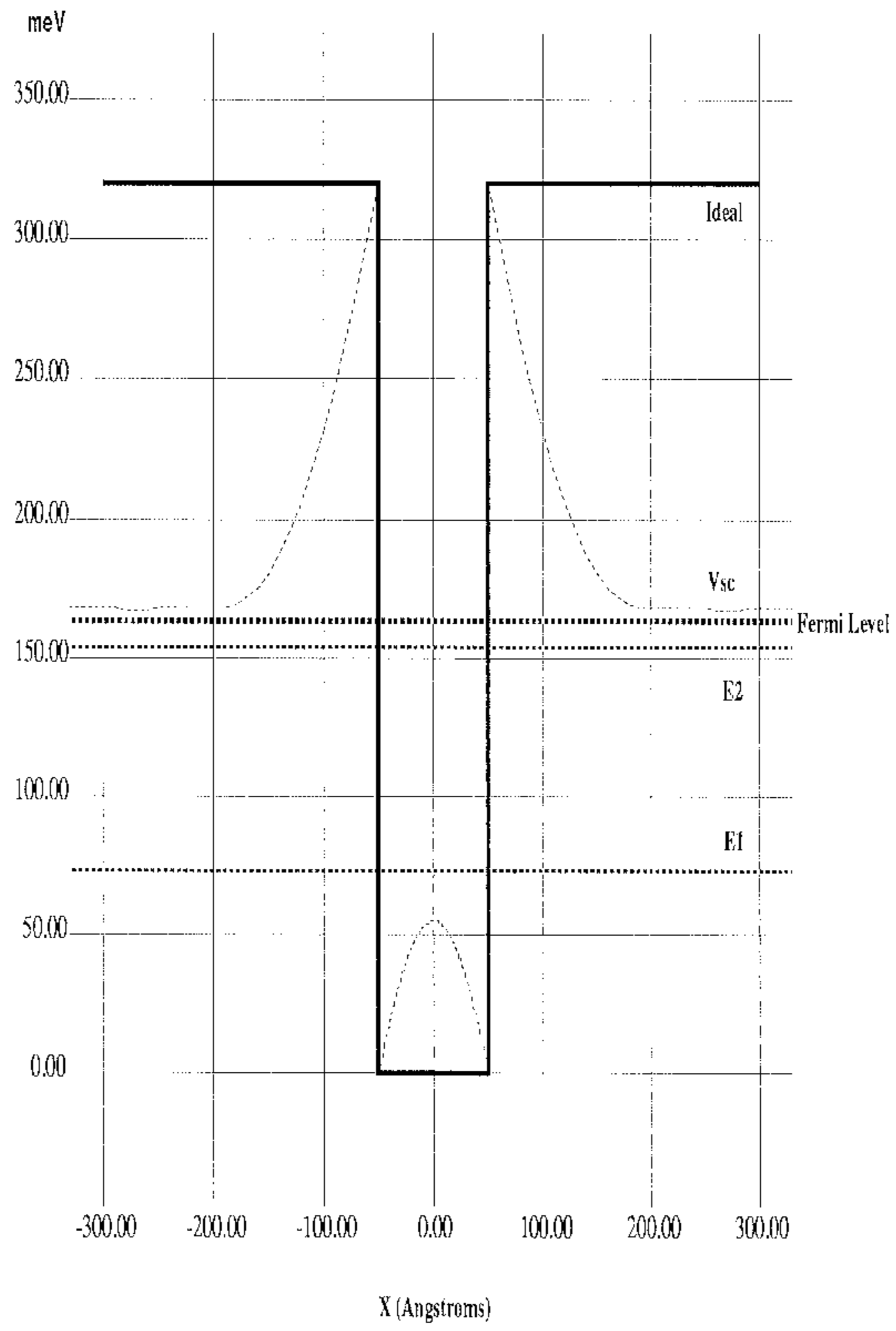
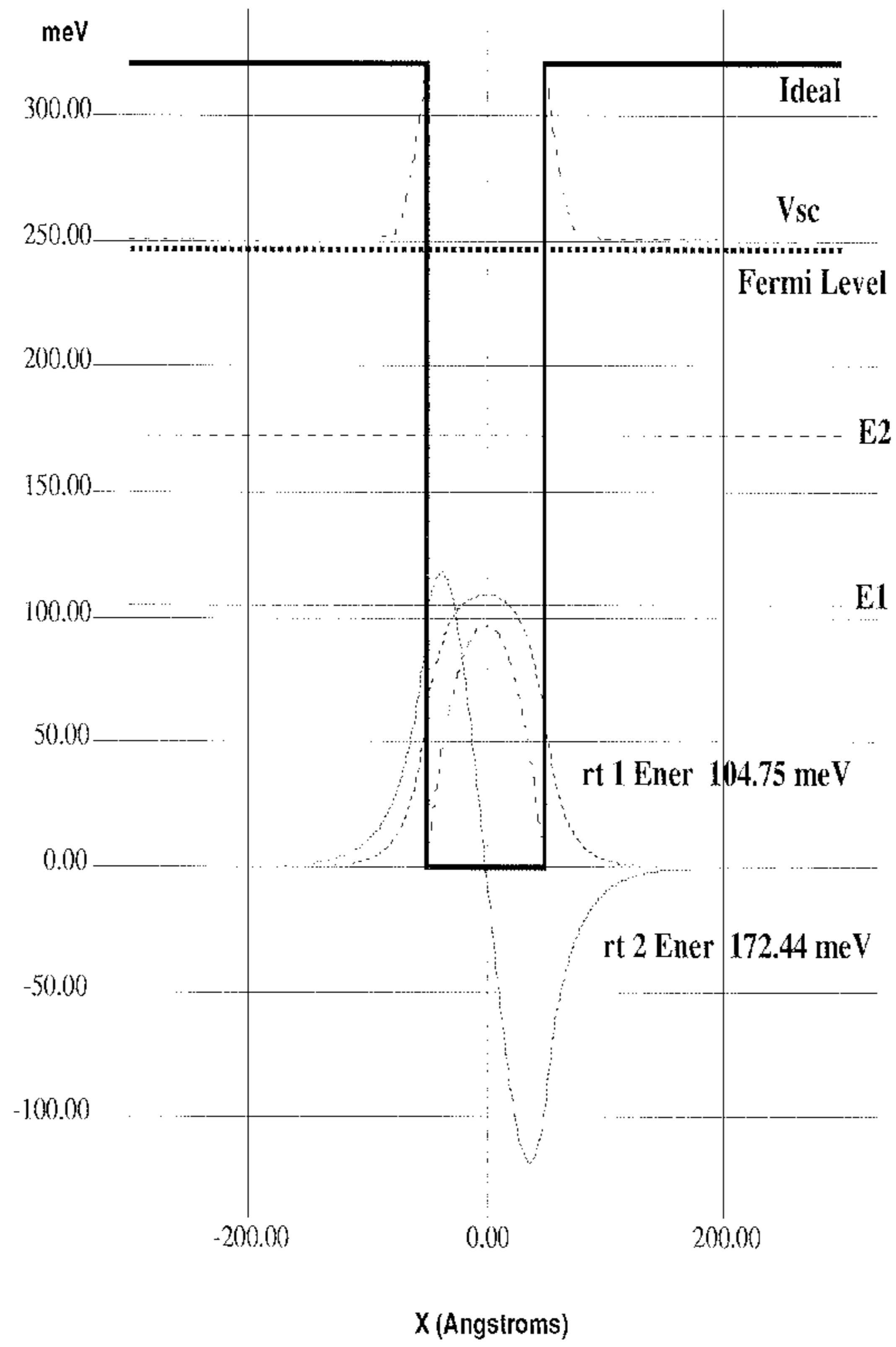


Figure 10: Quantum Well, Donor Density 10^{19}



6 Conclusions

We have introduced the Galerkin implementation of the finite element technique and used it to cast Poisson's equation into a form amenable to efficient, accurate numerical solution. The source terms for Poisson's equation have been developed and their continuity conditions described, and a formulation for finding a Fermi level to insure charge neutrality has been described. A general mathematical treatment of finite element method boundary conditions was presented. We have solved the Poisson and Schroedinger equations simultaneously until achieving a self-consistent solution. Results have been presented for a self-consistent 100 Å quantum well of GaAs and AlGaAs, constructed with a 320 meV bandgap, at a full range of donor densities. We have shown that the spacing between the first and second bound states decreases with increasing donor concentration, as we would expect from the behavior of the GaAs/AlGaAs superlattice detailed in the literature. We have discussed the surprisingly large depletion regions required to obtain a valid solution at low donor densities, and shown that we account for the complete depletion region while other solutions may not.

Our algorithm can readily solve for high donor densities which previous projects using different techniques were unable to attain. The solution can account for externally applied in-plane and perpendicular magnetic fields, as well as externally applied potentials. The device geometry and materials of construction can be selected. We can easily extend the procedure to nonzero temperatures.

Our solution demonstrates the power and flexibility of the finite element approach to solving differential equations. Our method can account for all of the variables mentioned simultaneously, and can do so accurately and efficiently. These techniques should allow us

to model nearly any device accurately and obtain energy levels and wavefunctions for direct experimental verification.

References

- [1] Tsuneya Ando. Self-consistent results for a GaAs/Al_xGa_{1-x}As heterojunction. I. Sub-band structure and light-scattering spectra. *Journal of the Physical Society of Japan*, December 1982.
- [2] Tsuneya Ando and Shojiro Mori. Electronic properties of a semiconductor superlattice. I. Self-consistent calculation of subband structure and optical spectra. *Journal of the Physical Society of Japan*, November 1979.
- [3] Richard P. Brent. *Algorithms for Minimization Without Derivatives*. Prentice-Hall, Englewood Cliffs, N.J., 1973. Chapters 3, 4.
- [4] Bruce C. Duncan. Self-consistent analysis of energy levels in modulation doped heterostructures. Senior Thesis. Worcester Polytechnic Institute, Worcester, MA, May 1990.
- [5] Kaoru Inoue and Hiroyuki Sakaki. A new highly-conductive (AlGa)As/GaAs/(AlGa)As selectively-doped double-heterojunction field-effect transistor (SD-DH-FET). *Japanese Journal of Applied Physics*, February 1984.
- [6] Kaoru Inoue, Hiroyuki Sakaki, Junji Yoshino, and Takashi Hotta. Self-consistent calculation of electronic states in AlGaAs/GaAs/AlGaAs selectively-doped double-heterojunction systems under electric field. *J. Appl. Phys.*, December 1985.
- [7] Kyeu T. Kim, Sang Soo Lee, and S. L. Chuang. Inter-miniband optical absorption in a modulation-doped Al_xGa_{1-x}As/GaAs superlattice. *J. Appl. Phys.*, May 1991.

- [8] S. E. Laux, D. J. Frank, and Frank Stern. Quasi-one dimensional electron states in a split-gate GaAs/AlGaAs heterostructure. *Surface Science*, 196, 1988.
- [9] Kenji Nakamura, Akira Shimizu, Masanori Koshiya, and Kazuya Hayata. Finite-element analysis of quantum wells of arbitrary semiconductors with arbitrary potential profiles. *IEEE Journal of Quantum Electronics*, May 1989.
- [10] L. Ramdas Ram-Mohan. Lecture notes on the transfer matrix method. Unpublished notes, June 1986.
- [11] L. Ramdas Ram-Mohan. Notes on gaussian quadrature. Unpublished notes, May 1989.
- [12] L. Ramdas Ram-Mohan. The finite-element method for energy eigenvalues of quantum mechanical systems. *Computers in Physics*, January/February 1990.
- [13] L. Ramdas Ram-Mohan. Observation of above-barrier quasi-bound states in asymmetric single quantum wells by piezomodulated reflectivity. *Submitted for publication*, 1991.
- [14] J. Sanchez-Dehesa, F. Meseguer, F. Borondo, and J. C. Mann. Self-consistent calculation of the electronic properties of a selectively doped $\text{Al}_x\text{Ga}_{1-x}\text{As}$ -GaAs quantum well under high magnetic fields. *Physical Review B*, September 1987.
- [15] A. M. Cruz Serra and H. Abreu Santos. A one-dimensional, self-consistent numerical solution of Schrodinger and Poisson equations. *J. Appl. Phys.*, September 1991.
- [16] P.M. Solomon, C. M. Knoedler, and S. L. Wright. A GaAs gate heterojunction FET. *IEEE Electron Device Letters*, September 1984.

- [17] Benjamin S. Staveley. Energy eigenvalues of charged carriers in quantum heterostructures in an externally applied magnetic field. Senior Thesis. Worcester Polytechnic Institute, Worcester, MA, May 1991.

- [18] Frank Stern and Sankar Das Sarma. Electron energy levels in GaAs-Ga_{1-x}Al_xAs heterojunctions. *Physical Review B*, July 1984.

- [19] Ikuo Suemune. Doping in a superlattice structure: Improved hole activation in wide-gap II-VI materials. *J. Appl. Phys.*, March 1990.

- [20] John Wilkins. Recent conversation.